

The sensitivity of Cherenkov telescopes to dark matter and astrophysical anisotropies in the diffuse gamma-ray background

Joachim Ripken,^{a,b} Alessandro Cuoco,^{a,c,d} Hannes-S. Zechlin,^{c,d,e}
Jan Conrad^{a,f} Dieter Horns^e

^aThe Oskar Klein Centre for Cosmo Particle Physics,
AlbaNova, SE-106 91 Stockholm, Sweden

^bMax-Planck-Institute for Solar System Research,
Max-Planck-Straße 2, D-37191 Katlenburg-Lindau, Germany

^cDepartment of Physics, University of Torino, via P. Giuria 1, 10125 Torino, Italy

^dIstituto Nazionale di Fisica Nucleare, via P. Giuria 1, 10125 Torino, Italy

^eUniversity of Hamburg, Institut für Experimentalphysik,
Luruper Chaussee 149, D-22761 Hamburg, Germany

^fWallenberg Academy Fellow

E-mail: ripken@mps.mpg.de, cuoco@fysik.su.se, zechlin@to.infn.it,
conrad@fysik.su.se, dieter.horns@physik.uni-hamburg.de

Abstract. In this article, the capability of present (H.E.S.S., MAGIC, VERITAS) and planned (CTA) ground-based Cherenkov telescope systems for detecting angular anisotropies in the diffuse gamma-ray background is investigated. Following up on a study of the impact of instrumental characteristics (effective area, field of view, angular resolution, and background rejection efficiency), the first part examines the influence of different observational strategies, i.e. whether a single deep observation or a splitting over multiple shallow fields is preferred. In the second part, the sensitivity to anisotropies generated by self-annihilating dark matter is studied for different common dark matter models. We find that a relative contribution of $\sim 10\%$ from dark matter annihilation to the extra-galactic diffuse gamma-ray background can be detected with planned configurations of CTA. In terms of the thermally-averaged self-annihilation cross section, the sensitivity of CTA corresponds to values below the thermal freeze-out expectation $\langle\sigma v\rangle = 3 \times 10^{-26} \text{ cm}^3\text{s}^{-1}$ for dark matter particles lighter than ~ 200 GeV. We stress the importance of constraining anisotropies from unresolved astrophysical sources with currently operating instruments already, as a novel and complementary method for investigating the properties of TeV sources.

ArXiv ePrint: [1211.6922](https://arxiv.org/abs/1211.6922)

Contents

1	Introduction	1
2	Optimizing the observational strategy	3
2.1	Simplified setup	3
2.2	Influence of the detector configuration	6
3	Benchmark instrumental setups and cosmic-ray backgrounds	9
4	Dark matter sensitivity	11
5	Conclusions	19
A	Error on the Poisson anisotropy	20
A.1	Simple calculation	21
A.2	More accurate calculation	21
B	Sensitivity using the intensity APS	22
C	Sensitivity using the fluctuation APS	23

1 Introduction

The study of gamma-ray anisotropies [1, 2] has recently provided new and complementary insights into the nature of gamma-ray sources and the extra-galactic diffuse gamma-ray background (EDGB) [3, 4]. Experimentally, EDGB means the residual large-scale isotropic emission measured at high galactic latitudes after subtracting the *galactic* diffuse emission. This emission arises mostly from the integrated contribution of unresolved extra-galactic sources and, possibly, from the annihilation or decay of dark matter (DM). A contribution from galactic sources is however also possible if their emission extends to sufficiently high galactic latitudes to produce an almost isotropic contribution. It has been argued, for example, that millisecond pulsars can give a contribution to the EDGB [5]. Similarly, also galactic DM could contribute to the EDGB, besides the extra-galactic one. The measured energy spectrum of the EDGB is, however, compatible with a simple featureless power law [3] so that complementary information, for example from anisotropy, can help isolating different contributions to this emission. The pattern of anisotropies has been studied with different techniques, mainly through its angular power spectrum (APS), as in [1, 2]. Likewise, the study of the 1-point probability distribution function (PDF) [6] and the cross-correlation with galaxy catalogues [7] provide complementary information.

It has been argued that dark matter self-annihilation or decay could leave a specific imprint on the anisotropy pattern and spectrum of the EDGB [8–19]. In fact, while the

emissivity of ordinary astrophysical sources scales with the inner source densities $\sim \rho$ (modulo a source-class dependent bias factor), the emissivity of self-annihilating DM scales with its density squared $\sim \rho^2$. Owing to this difference, self-annihilating DM could leave its signature in the angular power spectrum of the EDGB. This simple picture can be further complicated by the presence of unresolved point sources that produce a Poissonian-like APS, more closely resembling the DM one. Nonetheless, even if the astrophysical Poissonian term dominates the intrinsic clustering APS, revealing the astrophysical and dark matter APS to be similar, it is still possible to separate the two contributions by measuring their energy dependence, i.e. the *anisotropy energy spectrum* [14]. The different hypotheses about the origin of the EDGB can thus be tested by measuring both the angular power spectrum and its energy dependence.

In addition, theoretical predictions for the anisotropies generated by different gamma-ray source populations (e.g., blazars and galaxy clusters [20], millisecond pulsars [21], star-forming galaxies [22]) become available, extending our knowledge on this approach and its potential.

Gamma-rays are currently detected mainly with two techniques. Observatories in space, such as the Fermi Large Area Telescope (Fermi-LAT) [23], enable the detection of gamma-rays through pair conversion in the detector itself. With the Fermi-LAT, gamma-ray photons can be observed in the energy range from a few ten MeV up to a few hundred GeV, with an effective area close to 1 m^2 and a field of view (fov) of $\sim 1 \text{ sr}$. Fermi-LAT routinely operates in sky surveying mode, continuously mapping the entire sky within $\sim 3 \text{ h}$. Complementary, Cherenkov light emitted from air showers initiated by gamma-rays penetrating the upper atmosphere can be observed with ground-based telescopes, such as H.E.S.S. [24], MAGIC [25], and VERITAS [26], or the planned Cherenkov telescope array (CTA) [27, 28]. The effective collection area of ground-based instruments is typically of the order of 10^5 m^2 to 10^6 m^2 . The energy range of current experiments lies between 60 GeV and 100 TeV, but future realizations of this concept will lower the threshold to 10 GeV or even 5 GeV [29]. Contrary to Fermi-LAT, ground-based instruments only offer a relatively small fov of typically a few msr, so that all-sky scans are not feasible. Observations can only be pursued during darkness under the condition of a clear sky, reducing the duty-cycle to $\sim 1000 \text{ h}$ per year. Furthermore, the trigger rate is dominated by a large background of hadronic showers. Specific techniques are employed to reduce this background substantially. However, even after sufficient gamma-hadron separation, air showers induced by cosmic-ray electrons can still contribute significantly to the background at a few hundred GeV [30–33], hardly separable from photon-induced air showers. Despite the difficulties mentioned above, interesting scales for the investigation of anisotropies are typically very small (less than 1°), so that a small fov does not pose a serious limit for their study. The angular resolution of Cherenkov telescopes is typically better than 0.1° , i.e. multipoles in the range between 100 and 1000 can be easily resolved. At the same time, the background is expected to be isotropic at small scales and therefore no fundamental obstacle either.

In this paper, we investigate the capabilities of ground-based Cherenkov telescopes for measuring gamma-ray angular anisotropies. In section 2, we introduce a simplified

Monte-Carlo approach that is used to study the impact of instrumental characteristics (fov, angular resolution, and background rejection power) to the detection sensitivity for anisotropies. Given that a combined analysis of data collected from observations of several different targets would be most effective, we investigate the influence of the *observational strategy*, i.e. whether it would be advantageous or disadvantageous to split the data into several fov. In section 3, we list the instrumental setups that are used as benchmarks, and we provide estimates of the CR background rates expected for these configurations. Section 4 introduces a more realistic simulation setup and a sensitivity study to anisotropies from DM self-annihilation for different DM models. Final comments and discussion are provided in section 5.

2 Optimizing the observational strategy

2.1 Simplified setup

As a measure of anisotropy we use the angular power spectrum (APS) of fluctuations throughout this paper. Given a map $I(\vartheta, \varphi)$ on the sphere, the fluctuation map is defined as $\delta(\vartheta, \varphi) = I(\vartheta, \varphi)/\bar{I} - 1$, where \bar{I} denotes the mean value of I . Thus, by definition, the mean value of $\delta(\vartheta, \varphi)$ is 0. The fluctuation map $\delta(\vartheta, \varphi)$ is decomposed into spherical harmonics $Y_m^\ell(\vartheta, \varphi)$ as $\delta(\vartheta, \varphi) = \sum_{\ell m} a_{\ell m} Y_m^\ell(\vartheta, \varphi)$, where $a_{\ell m}$ denote the coefficients of the spherical harmonic decomposition, $\ell = 0, \dots, \infty$, and $m = -\ell, \dots, \ell$. The coefficients $a_{\ell m}$ define the APS by

$$C_\ell \equiv \langle |a_{\ell m}|^2 \rangle, \quad (2.1)$$

where $\langle \dots \rangle$ indicates the statistical ensemble average. Then, the quantity

$$\hat{C}_\ell = \sum_m \frac{|a_{\ell m}|^2}{2\ell + 1} \quad (2.2)$$

provides an unbiased estimator of the true power spectrum C_ℓ , i.e. $\langle \hat{C}_\ell \rangle = C_\ell$.

Note that apart from the dimensionless fluctuation APS the dimension-full APS of the map $I(\vartheta, \varphi)$ itself can be used. This is particularly useful for the analysis of real data sets (see [1]), but we refrain from further consideration.

In order to simulate event lists containing anisotropies, we generate sky maps with a given C_ℓ spectrum. C_ℓ can be interpreted as the width of the $a_{\ell m}$ distribution over m for a fixed ℓ . Assuming Gaussian fluctuations, the $a_{\ell m}$ coefficients for a fixed ℓ can be randomly chosen from a Gaussian distribution centered on 0 with a width $\sqrt{C_\ell}$. The phase is chosen equally distributed between 0 and 2π with the condition $a_{\ell m} = a_{-\ell m}^*$, to ensure fluctuation maps with real values. Twelve realizations of the $a_{\ell m}$ are generated for a given spectrum, and thus twelve independent fluctuation maps $\delta(\vartheta, \varphi)$. Moreover, we simulate maps with five different benchmark APS following a power law with slopes $s = 0.5, 1.0, 1.5, 2.0, 2.5$, i.e. $\ell(\ell + 1)C_\ell \sim \ell^s$. The angular resolution of the simulated sky maps is chosen to be 0.002° , corresponding to a maximum resolvable multipole $\ell = 9 \times 10^4$. The maps are normalized as $\delta'(\vartheta, \varphi) = (\delta(\vartheta, \varphi) - \delta_{\min})/(\delta_{\max} - \delta_{\min})$, in order to obtain a distribution between 0 and 1 to simulate events. Hence, the map δ' acts

as effective intensity map $I'(\vartheta, \varphi) \equiv \delta'(\vartheta, \varphi)$. We emphasize that the anisotropies of this effective intensity map are independent of the original $\delta(\vartheta, \varphi)$ normalization and always in the range $-1 < \delta I'/\bar{I}' < 1$ by definition, thus implying large fluctuations of the order of 100%. The setup has been optimized for the purpose of investigating instrumental effects on the APS. However, the setup is extended to a more realistic approach in section 4, allowing the choice of an arbitrary anisotropy level.

Based upon the template intensity maps $I'(\vartheta, \varphi)$, the simulation of events requires the definition of the following three parameters: σ_{fov} , the half-width of the camera acceptance, σ_{psf} , the width of the point-spread function (PSF), and the signal fraction f_{sig} , the ratio of signal events with respect to the sum of signal and background events. Event lists contain an anisotropic *signal* component and a *background* component. The latter is isotropic by definition. Both the camera acceptance and the PSF are assumed to follow Gaussian distributions.

Each event of a list is handled in three subsequent steps: The celestial position is chosen randomly according to the camera acceptance. Comparing a uniform deviate with f_{sig} , it is then decided whether the event is treated as a *signal* or a *background* event. If the event belongs to the background, the event is just retained. In the signal case, instead, a variate z is generated, following a normalized uniform distribution. If z is smaller than $I'(\vartheta, \varphi)$ at the event's position, the event is kept, otherwise it is rejected. Eventually, each event is randomly displaced from its original direction according to the PSF, in order to realize the convolution of the map with the PSF. If not particularly specified, an event list contains $N_{\text{ev}} = 10^7$ entries. We point out that this number is unrealistically high, even for CTA, and is used to isolate and emphasize instrumental effects only. Simulations with a more realistic number of signal and background events are provided in section 4.

We use the HEALPix software and pixelization scheme [35] to create and analyze count maps (with N_{pix} pixels) as well as to extract the APS. Before the analysis, a count map is cast into a fluctuation map

$$\delta''(\vartheta, \varphi) = \frac{N_{\text{pix}}}{N_{\text{ev}}} \left[\sum_{i=1}^{N_{\text{pix}}} x_i b_i(\vartheta, \varphi) \right] - 1, \quad (2.3)$$

where x_i denotes the number of events in pixel i , and $b_i(\vartheta, \varphi)$ equals 1 inside pixel i and 0 otherwise. In this way, $\delta''(\vartheta, \varphi)$ is normalized such that $\int d\Omega [1 + \delta''(\vartheta, \varphi)] = 4\pi$, where $d\Omega$ is the differential solid angle element in spherical coordinates. It should be noted that, strictly speaking, $\delta''(\vartheta, \varphi)$ represents a fluctuation map (i.e. $\langle \delta''(\vartheta, \varphi) \rangle = 0$) only in the case that the average is performed over the whole sky rather than over the region of interest where the counts are located. The normalization has been chosen to keep a simple form of the noise term in the recovered APS (see next section), i.e. $C_N = 4\pi/N_{\text{ev}}$, where no factors of $f_{\text{sky}} = \Omega_{\text{fov}}/4\pi$ are involved (Ω_{fov} denotes the solid angle of the fov). We remark that a direct analysis of a fluctuation map built from a raw count map is pursued, while in principle the fluctuation map built from the reconstructed flux map (the count map divided by the exposure of the experiment or the fov in our case) can be

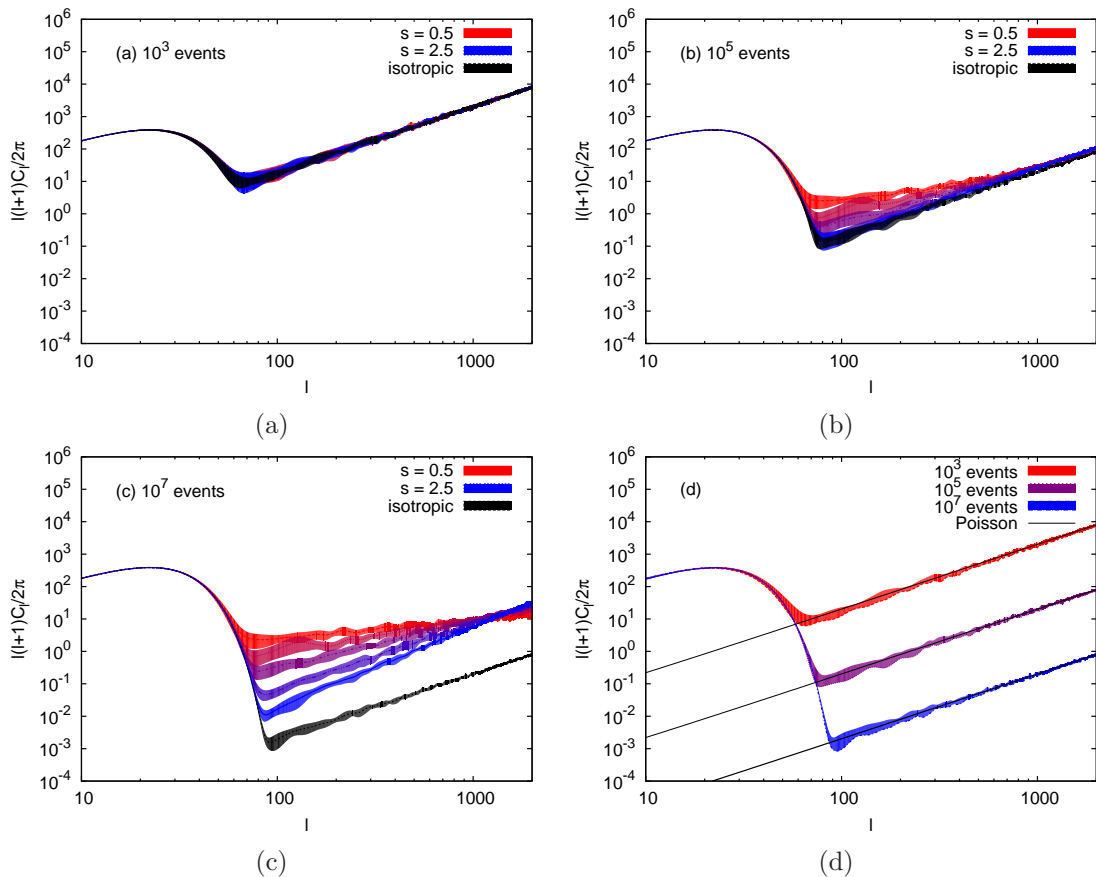


Figure 1: Angular power spectra measured from simulated event maps with different input APS slopes s between 0.5 and 2.5 in steps of $\Delta s = 0.5$ (from red to blue). The simulations contain signal-only events. The lower, black APS, labeled “isotropic”, refers to a background-only simulation with the same number of events. In this figure, PSF effects are neglected and $\sigma_{\text{fov}} = 2.5^\circ$. Sub-figures represent the cases of (a) 10^3 events, (b) 10^5 events, and (c) 10^7 events. The effect of an increasing event number on the Poissonian noise is depicted in (d), which shows together the APS of the background-only simulations from the panels (a), (b), and (c).

analyzed. While the latter is preferred for real data analyses, the former is sufficiently accurate for a sensitivity study. It implies the extracted APS to be a convolution of the experiment’s windowing function (the APS of the camera acceptance) with the true signal. For the large ℓ considered below, the windowing effect is marginal.

The statistical uncertainty of the APS is derived from the twelve simulations that have been performed for each case. In the following plots, the RMS as estimates of the standard deviation are shown as uncertainty bands.

2.2 Influence of the detector configuration

In figure 1, examples of APS measured from the simulated maps with given input-APS slopes are shown for a varying number of events. No background events have been included and all events are of signal type, except for the lowest, black APS, which is measured from a simulation containing background events only (an isotropic simulation). For small ℓ , the windowing function dominates the spectrum, which is distorted accordingly. For larger ℓ we see that the measured APS is the sum of the Poissonian noise and of the intrinsic APS. If the number of events is large enough, the different signal slopes can be easily discriminated. If the number of events is small, however, the random noise from the finite number of events prevails the measured APS. The Poissonian noise is given by $C_N = 4\pi/N_{\text{ev}}$ for full sky coverage (see appendix B in [10] and section IV.A in [8]), where $N_{\text{ev}} = N_{\text{sig}} + N_{\text{bg}}$ is the total number of events. This is in good agreement with the noise estimates from the background-only simulations (and partial sky-coverage corrected APS, see previous section), as shown in the lower right panel of figure 1. Since the Poissonian noise term is known, it is customary to remove it from the estimated APS so that to better show the intrinsic APS. We will discuss noise-subtracted APS for realistic simulations in section 4. The same considerations apply to the PSF effect and the background fraction discussed in the following, which can all be modeled, and thus corrected to give a final, unfolded APS. In the forward-folding approach used in section 4, these corrections are in principle not required, since the model is directly convolved with the PSF before comparison with the simulated data. Nonetheless, for illustration purposes, we show totally unfolded APS in section 4.

The effect of the instrument’s PSF on the measured APS is illustrated in the top-left panel of figure 2: The PSF suppresses the signal at large ℓ and drives it toward the level of the Poissonian noise. The characteristic multipole of the downturn is related to the PSF width σ_{psf} by $\ell_s \approx 180^\circ/\sigma_{\text{psf}}$. This effect can be corrected if σ_{psf} (or the full PSF shape in a non-Gaussian case) is known [1], however at the expense of an increasing uncertainty on the measured APS.

Anisotropies at an angular scale larger than the fov are suppressed. This effect is illustrated in the top-right panel of figure 2, where the APS of an isotropic (background-only) event list is shown for different fov. A larger fov allows exploring larger scales and thus lower multipoles. The minimum resolvable multipole is approximately given by $\ell_{\text{min}} \approx 180^\circ/\sigma_{\text{fov}}$.

The bottom panel of figure 2 illustrates the effect of different signal fractions f_{sig} . The background component mainly originates from two different processes:

- (i) Events caused by mostly isotropic cosmic rays (protons and electrons), which have been misclassified as photons. Anisotropies in the hadronic cosmic-ray background are indeed present at the level of 10^{-4} [38–42]. However, they extend to a multipole of ~ 20 only [38] and are thus negligible in our analysis. Anisotropies in the electron background have not been detected so far [36, 37]. For Cherenkov telescope systems the hadronic cosmic-ray background component dominates the gamma-ray signal. Therefore, a sufficiently good gamma-hadron separation is a crucial characteristic of the instrument. To reduce the residual background of cosmic-ray electrons,

which becomes important at energies below a few hundred GeV, a sufficiently good gamma-electron separation would be favorable as well. However, gamma-electron separation capabilities are limited due to the similarity of electron and photon initiated showers. With current instruments a rejection of $\sim 50\%$ of the electrons seems possible [32, 33], while the expected performance of CTA on this aspect has not been studied in detail yet.

- (ii) An intrinsically isotropic component of the diffuse photon background, which does not act as signal according to our definition. For instance, cosmological photons produced by truly diffuse processes may account for this component.

Note that we do not consider the effect of the local variations of the *night-sky background* and its effect on the camera acceptance [34]. Rather, we assume that prominent features in the fov such as bright stars can be eventually masked and excluded from the analysis. A more realistic MC simulation would be required to study this effect in detail. This is left for future work.

The bottom panel of figure 2 shows the measured APS for different signal fractions. A slope of $s = 0.5$ has been assumed for the input spectrum used to simulate the signal part of the maps and event lists. Dotted lines show the measured APS in the ideal case of vanishing PSF effects, vanishing fov distortion, and vanishing noise (but with background still included). As expected, the background fraction has a large impact and considerably reduces the signal height with respect to the intrinsic Poissonian noise, i.e. the signal-to-noise ratio. For the shown case of 10^7 events a signal fraction of 20% is still easily detectable. However, the signal-to-noise ratio decreases rapidly with decreasing f_{sig} , and for realistic cases f_{sig} can be as low as 0.1% while reaching a value of 2% in optimistic scenarios (see table 2 in section 4). We thus conclude that a good *background rejection* is crucial.

Finally, we investigate the effect of the observational strategy. In general, the detection of anisotropies requires a large amount of observation time. Thus, dedicated observations could eventually not be feasible, given different targets competing for the limited observation time available. The use of combined observations obtained on different targets would thus be preferable. This approach is investigated in figure 3. Here, a number of 10^3 , 10^5 , and 10^7 signal-only events are distributed within one fov as well as ten different ones. Qualitatively, when the same number of events is distributed in a single or multiple fov two competing effects arise: On the one hand, the density of signal events decreases since they are spread over a larger area, and thus the signal-to-noise ratio decreases (with our definition of the normalization of the maps, the Poissonian noise depends only on the number of events and it is the same in the single or multiple fov cases). On the other hand, multiple fov result in an increased number of modes available for the APS calculation, reducing the statistical error on the measured APS (on the sphere this effect is known as *cosmic variance*) and thus improving the sensitivity. The overall number of events eventually determines the dominating error and thus the dominating effect.

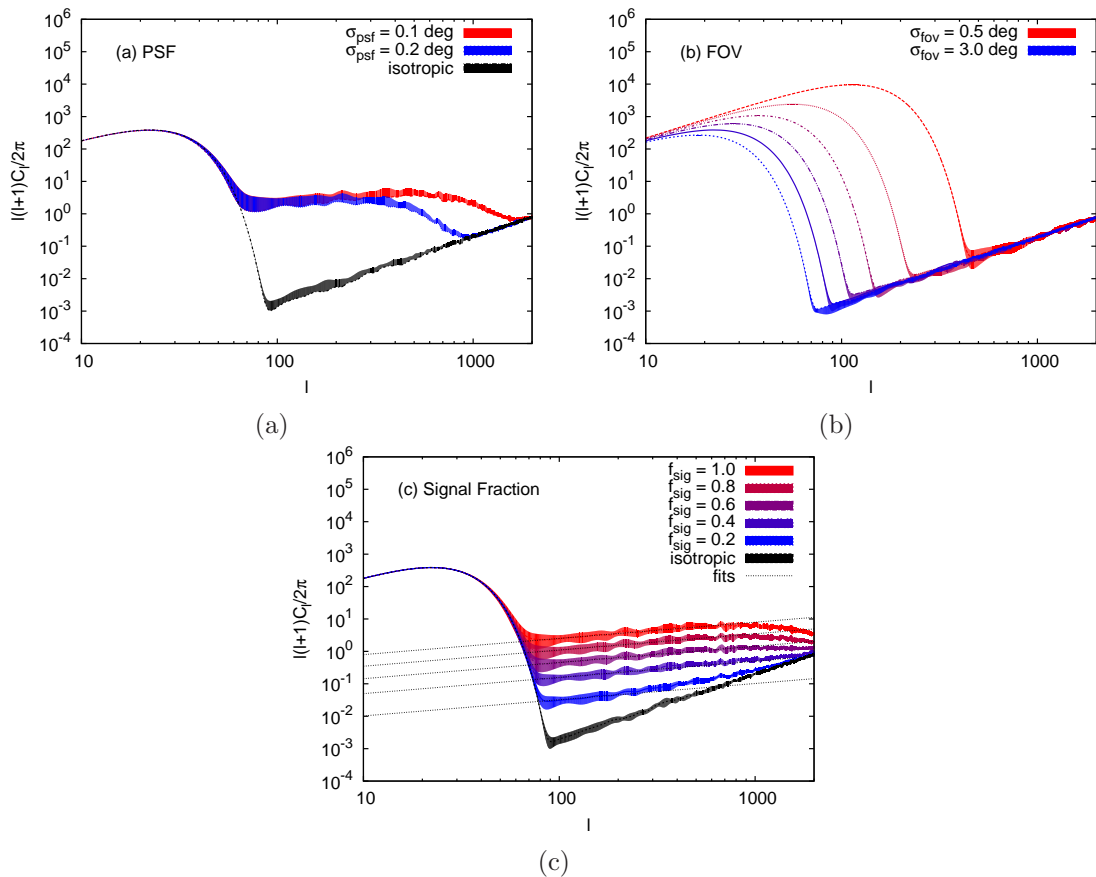


Figure 2: (a): influence of the PSF on the measured APS. The slope of the input spectrum is $s = 0.5$. The chosen PSF widths are $\sigma_{\text{psf}} = 0.1^\circ$ (red band) and $\sigma_{\text{psf}} = 0.2^\circ$ (blue band). (b): influence of the fov on the APS for a pure background (isotropic) event list, with $\sigma_{\text{psf}} = 0.05^\circ$. The width σ_{fov} is increased in steps of 0.5, in the range from $\sigma_{\text{fov}} = 0.5^\circ$ (red) to $\sigma_{\text{fov}} = 3.0^\circ$ (blue). (c): influence of the signal fraction f_{sig} on the measured APS for an input slope of $s = 0.5$; background events are distributed isotropically. Dotted lines show the APS in case of vanishing PSF, vanishing fov distortions, and vanishing noise.

As illustrated in figure 3, multiple fov indeed decrease the error on the measured APS and reduce the signal-to-noise ratio. The 10^7 -events case shows that a highly significant detection over all multipoles is achieved both in the single and multiple fov cases. On the other hand, the 10^5 -events case shows that while with the single fov observation a non zero APS can be detected up to a multipole of ~ 1000 , with the multiple fov case it is possible to significantly detect the anisotropy only up to a multipole of ~ 400 . In fact, while the error is decreased, the signal-to-noise ratio becomes too low to get a significant detection. Finally, in the 10^3 -events case there is no significant detection both in the single or multiple fov. A quantitative numerical study of this effect in a

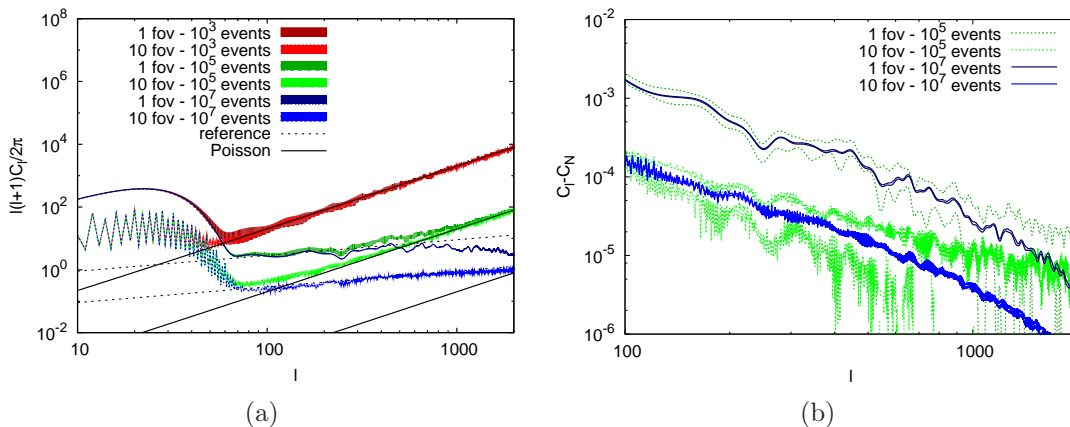


Figure 3: Impact of the observational strategy. (a): the measured APS for an input spectrum with a slope $s = 0.5$ is shown for 10^3 (red), 10^5 (green), and 10^7 (blue) signal-only events, distributed in a single fov (dark colors) or in ten different fov (light colors), respectively. Note that with our definition of the normalization of the maps, the Poissonian noise (depicted by the solid black lines) depends only on the number of events and it is the same in the single or multiple fov cases. For comparison, the thin dotted lines show the input APS for the two 10^7 -event cases. A Gaussian PSF with a width of 0.05° is assumed. (b): same as above, but showing the noise-subtracted power $C_\ell - C_N$ on the y -axis instead of $\ell(\ell + 1)C_\ell/2\pi$. The green (blue) lines enclose the 1σ error regions on the measured APS for 10^5 (10^7) events, distributed in a single (dark colors) or in ten different fov (light colors).

realistic scenario including background is presented in the section 4. Analytical formulae are derived in appendix A.

It should be stressed that the use of multiple fov requires the systematic error in the absolute calibration of each fov to be kept reasonably under control. In the following, we assume that this systematic error can be neglected compared to the statistical ones. A better assessment of this uncertainty will likely be available from future performance studies of CTA.

3 Benchmark instrumental setups and cosmic-ray backgrounds

Simulations of two instrument classes are presented in the following. The used instrumental setups are motivated by the characteristics of currently operating instruments such as H.E.S.S., MAGIC, and VERITAS, and the expected properties of CTA. Two different threshold energies (100 GeV and 300 GeV) have been adopted, revealing different signal-to-background ratios.

For currently operating instruments, the performance below 1 TeV typically degrades rapidly in energy. Hence, a threshold energy of 300 GeV is considered only. Above 300 GeV, an effective area of 10^5 m^2 (after selection cuts which improve the frac-

IACT	$E_{\text{thr}} = 100 \text{ GeV}$			$E_{\text{thr}} = 300 \text{ GeV}$		
	$A_{\text{eff}} [\text{m}^2]$	$\sigma_{\text{fov}} [\text{deg}]$	$\sigma_{\text{psf}} [\text{deg}]$	$A_{\text{eff}} [\text{m}^2]$	$\sigma_{\text{fov}} [\text{deg}]$	$\sigma_{\text{psf}} [\text{deg}]$
current	—	—	—	10^5	1.7	0.1
CTA	10^5	3, 4, 5	0.05	3×10^5	3, 4, 5	0.05

Table 1: Characteristics (effective area A_{eff} , field of view σ_{fov} , and PSF σ_{psf}) of the benchmark instrumental setups used in the simulations. The setups have been chosen in accordance with characteristics of current-generation IACTs and the planned CTA observatory. Predictions are made for two different threshold energies E_{thr} , 100 GeV and 300 GeV, respectively.

tion of gamma rays with respect to hadrons) is assumed. So is a fov of 1.7° and an angular resolution of 0.1° [24–26, 43].

For CTA, recent Monte-Carlo studies of the performance [27, 44, 45] indicate an effective area of $3 \times 10^5 \text{ m}^2$ above 300 GeV and 10^5 m^2 above 100 GeV (see figure 15 in [44]). In both cases, we assume an angular resolution of 0.05° (see figures 10 and 17 in [44]). The effective area as well as the angular resolution improve with energy, but the simulations have been considerably simplified choosing constant values close to the threshold energies, representing a conservative choice. For the fov, values between 3° and 5° are considered (see table 3 in [44]). We emphasize that a rather large fov of $\mathcal{O}(5^\circ)$ might be provided by the types C, D, and J of the suggested CTA arrays [44]. In addition, an effectively larger fov can be achieved with dedicated pointing patterns, adjusting the pointings of individual telescopes to correspondingly different offsets from a targeted position (see figure 3c in [27]). Table 1 summarizes the characteristics of the instruments used in this study. The performance of the recently built H.E.S.S.-II array is expected to lie in between the two setups considered here [43].

The intensity of the isotropic hadronic background component depends on analysis cuts and the quality of the gamma-hadron separation. With respect to present instruments, CTA will provide improvement in the performance of the hadron rejection process. However, a substantial part of the low-energy background is made by cosmic-ray electrons, which are more difficult to separate from gamma rays. The study in [44] provides a simulation of the total expected background from hadronic and leptonic components, which are used to estimate the background corresponding to our setups. In particular, we refer to their figure 16 of the integrated background rate per beam above a given energy threshold (and for the assumed effective area).

For a threshold energy of 100 GeV, a background rate of 0.01 Hz to 0.03 Hz per beam yields a total background rate of 50 Hz to 150 Hz for an angular resolution of $\sim 0.1^\circ$ and for a fov of 5° . Thus, benchmark background rates of 10 Hz and 100 Hz are assumed in this study, the first being slightly optimistic (but still possible depending on eventual improvements of the background rejection), and the second represents a more conservative choice. Rates for different fov scale with the factor $(\sigma_{\text{fov},1}/\sigma_{\text{fov},2})^2$. For simplicity, we use 10 Hz and 100 Hz as benchmark background rates for all considered fov, although these rates are over-estimated for smaller fov of 3° and 4° . The background

for a threshold of 300 GeV covers a range between 3×10^{-4} Hz and 3×10^{-3} Hz per beam, and the angular resolution covers values between 0.06° and 0.1° . For a fov of 5° , this corresponds to a total background rate of 1.5 Hz up to 42 Hz. Again, an optimistic and a more conservative background rate are chosen, i.e., 1 Hz and 10 Hz, respectively.

Assuming the same characteristics as for CTA for threshold energies above 300 GeV for current IACTs, the scaling to the correspondingly smaller fov reduces the background rate by a factor of 10. A further reduction in the rate is given by the smaller effective area. However, the background rejection capabilities are inferior with respect to the expectation for CTA, thus increasing the background rate. We use the same benchmark background rates as for CTA with threshold energies above 300 GeV, i.e. 1 Hz and 10 Hz. These values match typically observed background rates.

4 Dark matter sensitivity

A more realistic setup can now be employed to simulate maps with a given level of anisotropy. Here, we consider an anisotropy spectrum with a slope of $s = 2$ only, i.e. the same slope as of Poissonian noise. With the conventions given in section 2, $s = 2$ corresponds to an APS constant in multipole and can therefore be characterized by a single number, i.e. $C_\ell = C_P$ for all ℓ . This kind of anisotropy spectrum, known as Poisson anisotropy, is typically expected from unresolved point sources and provides a good approximation for most of the common DM scenarios [8, 9, 11–19]. The similarity to the Poissonian noise also suggests a straightforward way to simulate this kind of anisotropy: For N identical sources distributed all over the sky, the Poisson anisotropy of the fluctuation map will be $C_P = 4\pi/N$. Inverting the process, a map with an anisotropy equal to C_P can be simulated distributing $N = 4\pi/C_P$ equal sources on the sphere. This method is adopted in the following. In general, unresolved sources are not identical but have a certain flux distribution dN/dS , which typically follows a power law or broken power-law distribution. Anisotropy measurements can be used to recover the underlying dN/dS [2, 6]. To check our approximation of using an effective delta-like dN/dS , simulations for a realistic dN/dS have been performed, and are described later in this section. We follow the algorithm described in section 2 to produce a sequence of background or signal events from the simulated source maps. Different to section 2, the source maps are not rescaled, since they possess an intrinsic anisotropy normalization that we want to retain.

The total number of background events is given by the integrated background rates estimated in the previous section. The gamma-ray flux is normalized to the EDGB measured with Fermi-LAT: $\phi(E) = \phi_0 (E/100 \text{ MeV})^{-2.41}$, with $\phi_0 = 1.45 \times 10^{-7} \text{ cm}^{-2} \text{ s}^{-1} \text{ sr}^{-1} \text{ MeV}^{-1}$ [3]. Extrapolating the power-law spectrum above the considered threshold energies of 100 GeV and 300 GeV gives the integral fluxes $\phi(E > 100 \text{ GeV}) \approx 6 \times 10^{-10} \text{ cm}^{-2} \text{ s}^{-1} \text{ sr}^{-1}$ and $\phi(E > 300 \text{ GeV}) \approx 1.3 \times 10^{-10} \text{ cm}^{-2} \text{ s}^{-1} \text{ sr}^{-1}$. The effect of the EDGB attenuation expected from pair production on the extragalactic background light is neglected here. The expected softening is mild in most of the attenuation models [46–52], and taking it into account would only slightly reduce the total

flux above 100 GeV, while the attenuation could be more pronounced above 300 GeV. For a CTA observation of 100 h, this results in 10 448 and 6 659 signal events in total, assuming a fov of 5° and a threshold energy of 100 GeV and 300 GeV, respectively (setups as discussed in table 1). The events are distributed between DM and astrophysical sources according to the relative contribution to the EDGB as considered in the following. Changing the threshold energy from 100 GeV to 300 GeV, the number of gamma-ray events is reduced by less than a factor of 2, while the number of background events is reduced by a factor of 10 (due to their steeper energy spectrum and improved background rejection at higher energies). The signal-to-noise ratio of a given data set can thus be improved considering a threshold energy of 300 GeV. The numbers of gamma rays and background events for all the setups are reported in table 2.

The intrinsic anisotropy of astrophysical sources is modeled in accordance to the recent measurement of anisotropy performed with Fermi-LAT in the range of 1 GeV to 50 GeV [1]. The fluctuation energy spectrum of the measured anisotropy is compatible with a constant value of $\sim 10^{-5}$, while the *intensity* energy spectrum of anisotropy is compatible with a power law with slope ~ 2.4 . In combination, these results indicate that the measured anisotropy originates from unresolved blazars. This is further supported by the analysis performed in [2]. We assume that the result holds above 100 GeV. Thus, a value of $C_P^A = 10^{-5}$ is used for the intrinsic astrophysical source anisotropies. However, also other values of C_P^A will be explored to assess the robustness of the results with respect to the choice of this parameter.

The theoretical predictions for the intrinsic DM anisotropy are uncertain and span over a few orders of magnitude ranging from 10^{-4} to 10^{-1} . We assume a benchmark value $C_P^{DM} = 10^{-3}$ and will comment on other values in the following. A simplified analytic calculation is reported in the appendices A, B and C, illustrating the expected dependence of the sensitivity on the choice of C_P^{DM} and C_P^A .

To estimate the sensitivity to the DM component, we vary the relative contribution of DM to the total EDGB flux, assigning the remaining flux to the astrophysical component. In particular, we simulate 20 values of the DM contribution p from 0% to 100% in steps of 5%. The average astrophysical spectrum C_ℓ^A , its error σ_{C_ℓ} , and the average spectrum $C_\ell^{A+DM,p\%}$ composed of both the astrophysical and a fractional DM contribution of p are estimated from 20 realizations each. Note that C_ℓ^A indicates the *measured* average APS as function of the multipole ℓ . Ideally, assuming that no biases are present in the simulation pipeline, and after correcting for the instrumental effects, the CR background, and the Poisson noise, we should observe that $\langle C_\ell^A \rangle = C_P^A$ for all ℓ , where $\langle \dots \rangle$ indicates the average over many simulations. The same consideration applies to $C_\ell^{A+DM,p\%}$.

To quantify the sensitivity to the relative DM contribution, we use a simple chi-square approach, comparing two different definitions:

$$\chi_i^2(p) = \sum_{\ell=100}^{1000} \left(\frac{C_\ell^{A+DM,p\%} - C_\ell^{A,i}}{\sigma_{C_\ell}} \right)^2, \quad (4.1)$$

$$\chi_j^2(p) = \sum_{\ell=100}^{1000} \left(\frac{C_{\ell}^{\text{A+DM},p\%,j} - C_{\ell}^{\text{A}}}{\sigma_{C_{\ell}}} \right)^2, \quad (4.2)$$

where $C_{\ell}^{\text{A+DM},p\%,j}$ and $C_{\ell}^{\text{A},i}$ are the spectra from the single realizations as opposed to the average ones, $C_{\ell}^{\text{A+DM},p\%}$ and C_{ℓ}^{A} , respectively. Only multipoles above 100 are used, discarding lower multipoles affected by the fov of the instrument. The quantity $\chi^2(p)$ follows a chi-square distribution with 901 degrees of freedom, so that we can quote sensitivities at 95% confidence level (CL) for the value of p corresponding to a $\chi^2(p)$ larger than 972. Given that $\chi^2(p)$ scatters among different realizations, an additional criterion must be specified. For example, the average value of $\chi_i^2(p)$ over i can be used. Here, we adopt the more conservative requirement that at least 19 out of the 20 different $\chi_i^2(p)$ values (for a given p) are larger than the sensitivity threshold of 972, in order to set the value of p corresponding to the 95% CL. The two different ways to define $\chi^2(p)$, see Eqs. (4.1) and (4.2), correspond to two different definitions of the sensitivity. In the first approach, we assume and simulate a “true” case without a DM component and search for the minimum (at 95% CL) DM fraction required to exclude the null hypothesis. In the second approach, we assume and simulate “true” cases including a DM contribution of p and search for the minimum contribution for which the null hypothesis becomes incompatible with the simulated data. Both cases are found to give consistent results. We point out that the definition of sensitivity used here is in short a “95% CL incompatibility with the null hypothesis”, which implies a comparison of two χ^2 -distributions. Another commonly employed definition of a sensitivity as “95% upper limit in the case of a null detection outcome of the experiment” (which requires interval estimation through a profile likelihood or test statistic procedure) can give more stringent sensitivities, but is not considered in this work.

Finally, it should be noted that the sensitivity estimation described above assumes previous knowledge of the intrinsic astrophysical and DM anisotropies. In realistic cases, a measurement of these quantities from the analysis itself would be preferable in order to perform a comparison with the model predictions. This can be done, in practice, analyzing the data in multiple energy bands. The presence of more components at different energies and the intrinsic anisotropies of the components can then be inferred from a study of the anisotropy energy spectrum in intensity and fluctuation [14, 18]. We do not pursue such detailed analysis here, while for the sensitivity estimate to the DM contribution the above approach is sufficiently accurate.

The results are shown in table 2. Clearly, current instruments have limited prospects of constraining DM through small-scale angular anisotropies. It is worth stressing, nonetheless, that anisotropy searches also constrain population properties of astrophysical sources (as discussed in more detail below), so that this particular result should not hamper a dedicated search for anisotropies with current observatories. However, prospects for DM searches improve for CTA, especially if the background rate can be kept reasonably low. Sensitivities of $\sim 20\%$ and $\sim 10\%$ at 100 GeV and 300 GeV, respectively, can be achieved with single-target observations of 1000 h. Even in the most conservative case of a fov of 3° , a sensitivity of $\sim 30\%$ above 300 GeV can still be

H.E.S.S./MAGIC/VERITAS $E_{\text{th}}=300$ GeV $\sigma_{\text{fov}} = 1.7^\circ$

Observation time [h]	Bg. rate [Hz]	Sens.	N_{sig}	N_{bg}
100	1	$\gtrsim 100\%$	257	3.6×10^5
	10	$\gtrsim 100\%$		3.6×10^6
300	1	$\gtrsim 100\%$	770	1.08×10^6
	10	$\gtrsim 100\%$		1.08×10^7
1000	1	$\gtrsim 100\%$	2567	3.6×10^6
	10	$\gtrsim 100\%$		3.6×10^7
10×100	1	$\gtrsim 100\%$	2567	3.6×10^6
	10	$\gtrsim 100\%$		3.6×10^7

CTA $E_{\text{th}}=100$ GeV

Observation time [h]	Bg. rate [Hz]	$\sigma_{\text{fov}} = 4^\circ$		$\sigma_{\text{fov}} = 5^\circ$		N_{bg}
		Sens.	N_{sig}	Sens.	N_{sig}	
100	10	90%	6687	70%	10448	3.6×10^6
	100	$\gtrsim 100\%$		$\gtrsim 100\%$		3.6×10^7
300	10	45%	20059	35%	31343	1.08×10^7
	100	$\gtrsim 100\%$		$\gtrsim 100\%$		1.08×10^8
1000	10	30%	66867	20%	104476	3.6×10^7
	100	95%		75%		3.6×10^8
10×100	10	55%	66867	40%	104476	3.6×10^7
	100	$\gtrsim 100\%$		$\gtrsim 100\%$		3.6×10^8

CTA $E_{\text{th}}=300$ GeV

Observation time [h]	Bg. rate [Hz]	$\sigma_{\text{fov}} = 4^\circ$		$\sigma_{\text{fov}} = 5^\circ$		N_{bg}
		Sens.	N_{sig}	Sens.	N_{sig}	
100	1	55%	4262	30%	6659	3.6×10^5
	10	$\gtrsim 100\%$		95%		3.6×10^6
300	1	30%	12785	20%	19976	1.08×10^6
	10	80%		60%		1.08×10^7
1000	1	15%	42617	10%	66587	3.6×10^6
	10	45%		30%		3.6×10^7
10×100	1	30%	42617	20%	66587	3.6×10^6
	10	85%		65%		3.6×10^7

Table 2: Sensitivity for detecting a self-annihilating DM contribution to the EDGB, utilizing anisotropy measurements in terms of the angular power spectrum. The sensitivity is given in terms of the minimum detectable DM gamma-ray flux, expressed in percentages of the EDGB. The three tables list the sensitivities for instrumental setups resembling current IACTs and the planned CTA, respectively, for several observation times, background rates, fov, and observational strategies. For reference, the number of simulated signal (N_{sig}) and background (N_{bg}) events is listed. A value of $\gtrsim 100\%$ refers to a sensitivity outside our tested range.

reached with CTA (not shown in the table), while a fov of 4° would result in a sensitivity of $\sim 15\%$.

Facing realistic data sets, the change in sensitivity for different observational strate-

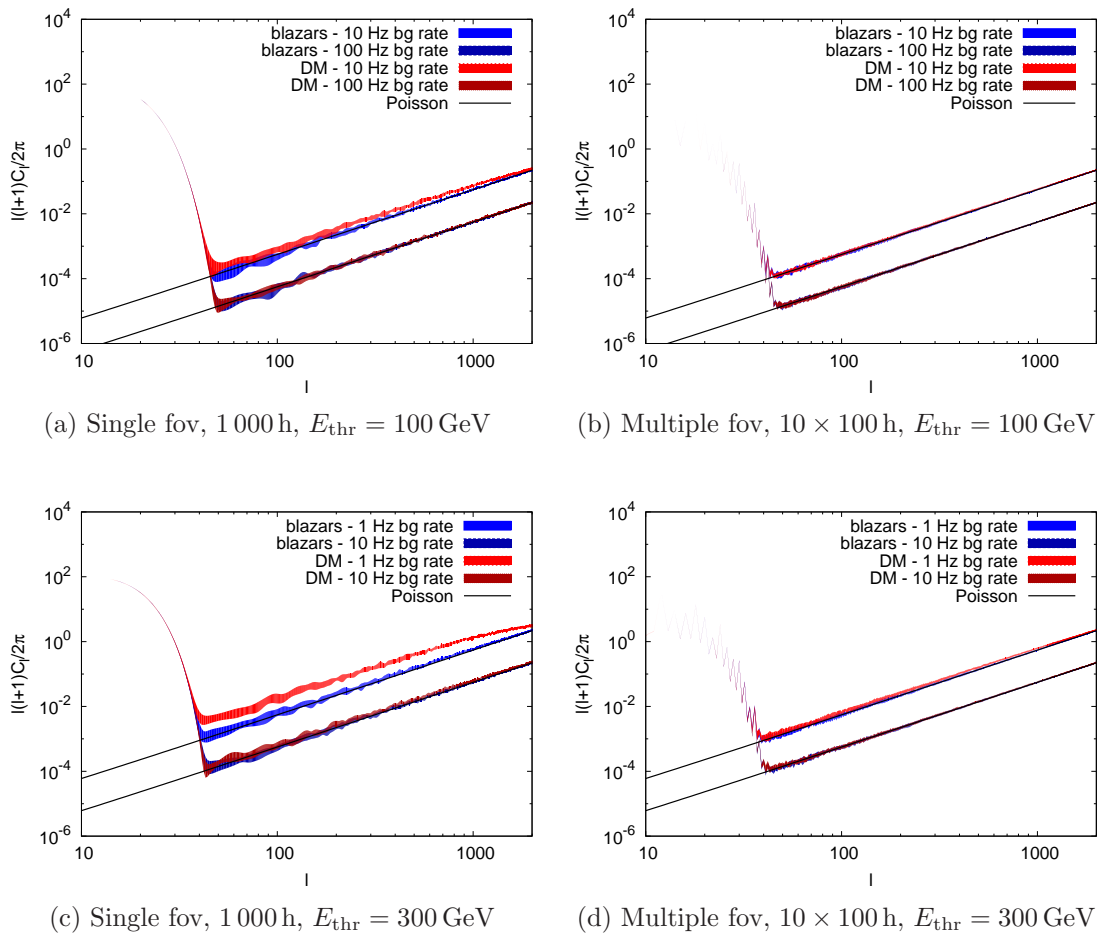


Figure 4: Comparison between the measured APS for a pure astrophysical case with $C_\ell = C_P^A = 10^{-5}$ (blue bands) and a case with 40% of the total radiation originating from self-annihilating DM with $C_\ell = C_P^{DM} = 10^{-3}$ (red bands). An observation with a CTA-like telescope system of 1 000 h on a single target (left column) and of 10×100 h splitted on ten different targets (right column) is considered. The upper plots refer to an energy threshold of 100 GeV and the lower ones refer to a threshold of 300 GeV. The two cases in each panel refer to background rates of 10 Hz and 100 Hz for 100 GeV, and 1 Hz and 10 Hz for 300 GeV. The size of the fov is $\sigma_{\text{fov}} = 5^\circ$. The lines show the estimated noise levels.

gies is worth mentioning. As shown in table 2, the sensitivity for a combination of ten different observations of 100 h each is just a factor of 2 worse compared to a continuous 1 000 h single target observation. In addition, the sensitivity of the combined data set is approximately equivalent to a full 300 h observation of a single target. Following the discussion at the end of section 2.2 we see that, even with CTA, the statistical regime where a multiple-fov strategy results in a reduction of the errors cannot be reached.

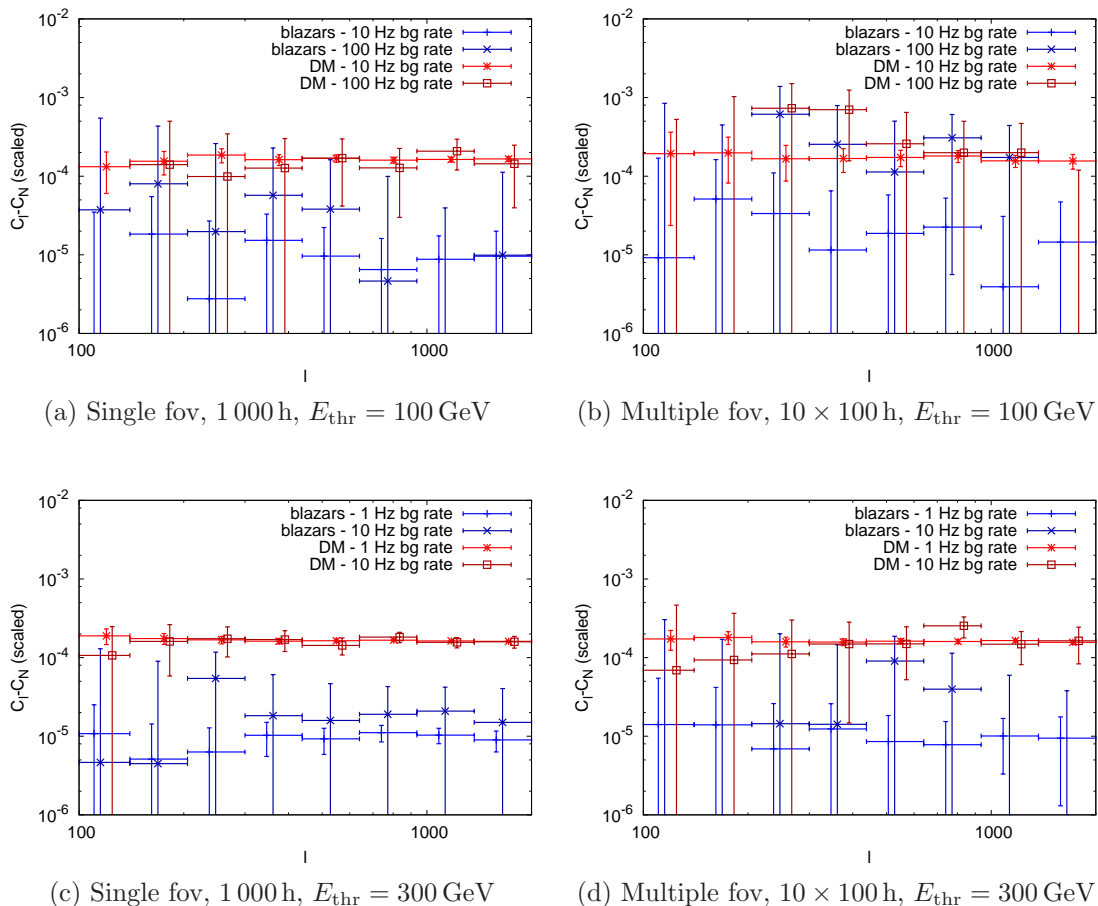


Figure 5: Same as figure 4, but showing the noise-subtracted and instrumental effects unfolded APS. Note that, in difference to figure 4, the y -axis shows $C_\ell - C_N$ instead of $\ell(\ell + 1)C_\ell/2\pi$. Also, the APS are binned into 8 logarithmically spaced bins in ℓ . See text for more details. For readability, the bins for each sub-case in each plot are slightly shifted.

Rather, the combination of multiple fov results in errors comparable or slightly larger than the single fov observation. Nonetheless, observations of single targets for 1 000 h each are practically not feasible (perhaps apart from the Galactic Center over several years), and the observation of ten different targets for 100 h each is more likely to be realized. We emphasize that these observations do not need to specifically target anisotropy searches, but observations taken for different purposes can be analyzed instead. In this manner, the loss in sensitivity by a factor of ~ 2 is compensated by the availability of a significantly larger data set.

As a specific example of our analysis, figures 4 and 5 show the APS for the cases of 1 000 h and 10×100 h of observation time with CTA for the threshold energies of 100 GeV and 300 GeV, and a fov of 5° . The pure astrophysical case ($C_P^A = 10^{-5}$) and a case of a

40% DM ($C_P^{DM} = 10^{-3}$) contribution are shown, as well as the two different choices of background rates. Figure 4 shows the raw measured APS and illustrates the fact that the variance of the APS decreases when the observation time is splitted over several fov, but, at the same time, the signal over noise ratio also decreases. Further informations are difficult to infer from figure 4. For this reason unfolded and binned APS are shown in figure 5. Unfolding involves subtraction of the Poissonian noise and correction for the PSF attenuation. In the simple case of a Gaussian beam, which we adopted, the PSF correction is simply given by the factor $w_\ell^2 = \exp(\sigma_{\text{psf}}^2 \ell(\ell+1))$, see [1, 8] and appendix A. The presence of the background also alters the normalization of the APS. This effect can be corrected by rescaling the noise-subtracted APS by the factor $N_{\text{ev}}^2/N_{\text{sig}}^2$. Clearly, this correction requires a perfect, and thus unrealistic, knowledge of the fraction of signal and background in the collected data, while this information will likely be available with a large error only. However, this will not pose a problem in the analysis of real data, where the *intensity* APS is used instead of the dimensionless APS and no a priori knowledge of the gamma-ray flux is required. Finally, the limited fov also introduces a re-normalization of the APS by a factor f_{sky} which we corrected in the unfolding. A binning of data is implemented given the large error for a single multipole. Since C_ℓ coefficients of neighboring multipoles are correlated, the knowledge of the full covariance matrix is in principle necessary to calculate the error after binning. Here, we use a simple analytical estimate of the error, which is given by $\delta C_{\bar{\ell}} = (C_{\bar{\ell}} + C_N w_{\bar{\ell}}^2) \sqrt{2/(2\bar{\ell} + 1)/\Delta\ell/f_{\text{sky}}}$, where $\Delta\ell$ is the width of the bin, $\bar{\ell}$ is the average ℓ of the bin, and $w_\ell = \exp(\sigma_{\text{psf}}^2 \ell(\ell+1)/2)$. This approach is accurate for all but very low ($\ell < 10$) multipoles. The unfolded APS of figure 5 show that we recover within the errors the input anisotropy $C_P^A = 10^{-5}$ for the astrophysical case and the anisotropy $C_P^{A+DM,40\%} = 0.4^2 \cdot C_P^{DM} + 0.6^2 \cdot C_P^A \simeq 1.6 \times 10^{-4}$ for the case of 40% DM. It can be also seen from the plot that, when the background rate increases, the input signal can still be recovered although, as expected, with a larger error. The case of ten fov observations explicitly shows that the errors worsen by approximately a factor of 2 in agreement with the results of table 2. The sensitivity to DM inferred from figure 5 is in line with the values reported in table 2.

The other crucial parameters determining the sensitivity are C_P^{DM} and C_P^A . To test the dependence on these parameters, we performed a further simulation with $C_P^A = 10^{-4}$ (instead of $C_P^A = 10^{-5}$), keeping the value $C_P^{DM} = 10^{-3}$, and we found the sensitivities to decrease by a factor ~ 3 . This seems to be in good agreement with the analytic scaling relation $(C_P^A/C_P^{DM})^{1/2}$ found in the appendix. Given the strong dependence on these two parameters, a firmer prediction of the sensitivity requires pinning down their uncertainties. More accurate calculations of C_P^{DM} have been recently reported in [19], indicating that C_P^{DM} can be as high as 10^{-1} , dominated by the contribution of the galactic substructures over extragalactic ones (see in particular their figure 7). Although such a large DM anisotropy would push the sensitivity to values better than 1%, the intrinsic emission from these very anisotropic structures is expected to be very low, as witnessed by the fact that the *intensity* anisotropies are instead dominated by the extragalactic component (see [19]). The results presented in [19] also indicate that the DM APS is not exactly flat in multipole, but shows a slight attenuation to higher mul-

tipoles. Given the good angular resolution of CTA, this effect can in principle be used to disentangle the DM contribution from the astrophysical one. However, the detection of a non-zero anisotropy will likely be at a low signal-to-noise ratio, therefore it will be difficult to explore large ℓ since they will be noise-dominated. The effect is also somewhat degenerated with the PSF attenuation and will thus require a good calibration of the instrumental performance. A more accurate estimate of C_P^A , instead, awaits a direct measurement with Cherenkov telescopes or further work on the modeling of blazar populations at TeV energies. In this respect, the examples depicted in figures 4 and 5 show that the observation of an anisotropy $C_P^A = 10^{-5}$ is close to the sensitivity attainable with 1000 h of observation time with CTA (for the optimistic background estimate), while it would be more challenging for the splitted observation strategy. However, C_P^A is not precisely known, and the possibility of a larger power such as 10^{-4} would obviously improve its detection capabilities, albeit implying a lower DM sensitivity. We thus propose explicit observations of these kind of anisotropies even with the current generation of instruments. Besides the possibility of constraining a DM contribution, an observation of anisotropy would provide a complementary and powerful tool to investigate astrophysical TeV sources.

We checked that the results are robust with respect to the approximation of a delta-like source flux distribution dN/dS , as opposed to a more realistic distribution, which typically shows a power law or a broken power-law behavior (see for example [53]). We simulated the case of a power-law distribution $\propto S^{-2.4}$ for both DM and astrophysical sources, spanning two orders of magnitude in flux and normalized to give the same level of anisotropy as in the delta case, i.e. $C_P^A = 10^{-5}$ and $C_P^{DM} = 10^{-3}$. The resulting sensitivities are identical to the delta-like case. This result is perhaps not surprising, since the anisotropy C_P is given by an integral over dN/dS below the point-source detection threshold S_{lim} , more precisely $C_P = \int_0^{S_{\text{lim}}} dS S^2 dN/dS$, so that different dN/dS distributions can still result in the same C_P .

The sensitivities given in table 2 as fraction of the EDGB flux can be expressed in terms of the more common quantity of the velocity-averaged DM self-annihilation cross section $\langle\sigma v\rangle$, although this introduces further model dependence. To normalize the DM signal, we use the cosmological DM model of [54] in its optimistic version, where DM halos are modeled with NFW profiles and include the presence of DM subhalos, boosting the annihilation signal further (see, e.g., [55, 56] for gamma-ray implications of galactic DM subhalos). In addition, the less optimistic version neglecting DM subhalos is considered, resulting in a factor of ~ 10 less DM annihilation flux and thus a correspondingly worse sensitivity. It should be noted that considering the results of [16] from the Millennium-II simulation, an order of magnitude enhancement with respect to the above “optimistic” case is predicted with a correspondingly improved sensitivity (see also [57], in particular figure 1). The results are shown in figure 6 for various annihilation channels as function of the DM particle mass m_χ . In conclusion, the self-annihilation cross section $\langle\sigma v\rangle = 3 \times 10^{-26} \text{ cm}^3\text{s}^{-1}$ expected from thermal dark matter freeze-out can be probed with CTA for DM particle masses up to a few hundred GeV. Interestingly, even using the conservative version of the EDGB DM model above, sensitivities

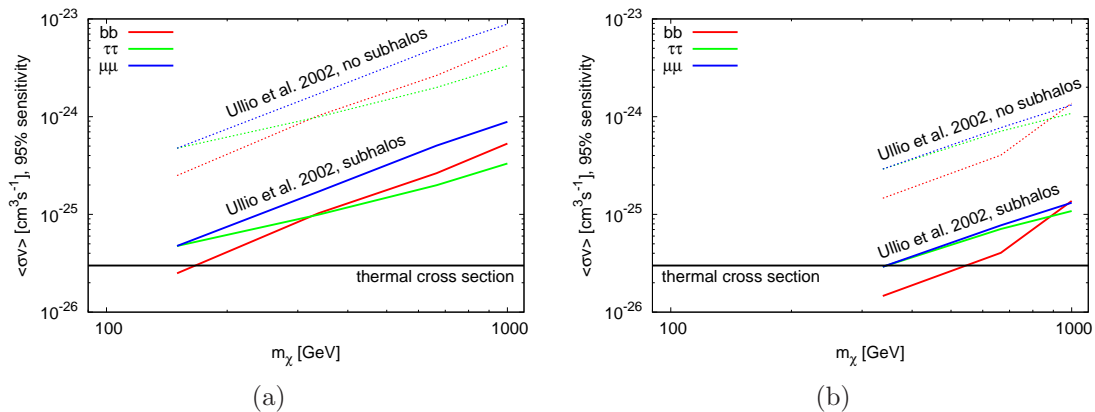


Figure 6: (a): sensitivity of CTA on the velocity-averaged DM self-annihilation cross section $\langle\sigma v\rangle$ as a function of the DM particle mass m_χ , for an energy threshold of 100 GeV, 300 h (or 10×100 h) of observation time, $\sigma_{\text{fov}} = 5^\circ$, and a background rate of 10 Hz (corresponding to a contribution from self-annihilating DM of $\sim 35\%$ to the total EDGB, see table 2). Solid lines correspond to the model of [54], i.e. incorporating DM annihilation in subhalos, while dotted lines refer to the more conservative case of absent DM subhalos, giving a sensitivity by approximately a factor of 10 worse. We consider DM annihilation in $b\bar{b}$ (red), $\tau^+\tau^-$ (green), and $\mu^+\mu^-$ (blue) final states. Assumed instrumental characteristics are discussed in the text. (b): same as above for an energy threshold of 300 GeV, 300 h (or 10×100 h) of observation time, and a background rate of 1 Hz (corresponding to a contribution from self-annihilating DM of $\sim 20\%$ to the total EDGB, see table 2).

better than the ones achievable with dwarf spheroidal galaxies observed with CTA and comparable with achievable limits using cluster observations can be reached [28].

5 Conclusions

We have investigated the key aspects of the capability of ground-based gamma-ray telescopes with small fields of view (i.e. imaging atmospheric Cherenkov telescopes) for observing anisotropies in the diffuse gamma-ray background. In particular, the effects of the effective area, the field of view, the angular resolution (PSF), and of the hadron-background rejection efficiency have been studied. These properties have been identified as crucial instrumental characteristics, determining the sensitivity for detecting small-scale angular anisotropies.

The sensitivity for detecting a contribution of self-annihilating dark matter to the diffuse gamma-ray background has been investigated, focussing on the analysis of angular anisotropies. Benchmark instrumental setups of currently operating imaging atmospheric Cherenkov telescopes such as H.E.S.S., MAGIC, and VERITAS, as well as the forthcoming CTA have been considered. We have used realistic expectations for the anisotropy power spectra from self-annihilating dark matter and from astrophysical

sources. We find that the sensitivity of CTA will be sufficient to resolve a relative contribution of $\sim 10\%$ from self-annihilating dark matter to the total isotropic gamma-ray background flux, given an observation time of 1000 h and a background rate of 1 Hz above 300 GeV. More important, we find that with a multiple field-of-view strategy of 1000 h of observation time splitted over ten separate targets of 100 h each yields a slight reduction in sensitivity (to $\sim 20\%$, a factor of 2) only. In practice, this means that it will be possible to obtain interesting constraints on dark matter without dedicated deep observations, but combining existing observations of different primary astrophysics targets. The sensitivity achievable can be already sufficient to probe the thermal annihilation cross section for WIMP masses $\lesssim 200$ GeV (for common models of dark matter annihilation in galactic and extragalactic environments). We also find that CTA will have sufficient sensitivity for detecting small-scale anisotropies from astrophysical sources with a Poissonian anisotropy level of 10^{-5} , while the sensitivity of current-generation instruments is approximately an order of magnitude lower. Given the uncertainty on the exact expected anisotropy level, we propose that available deep exposures, preferably at high galactic latitudes, should be analyzed in order to search for anisotropies. An observation of anisotropy would provide a complementary and invaluable tool for investigating the nature of TeV sources.

Acknowledgments

We wish to thank Mattia Fornasa and Jesus Zavala for providing suggestions on the manuscript and for useful discussions. We kindly thank the anonymous referee for useful and important suggestions on improving the manuscript. DH acknowledges support through the collaborative research center (SFB) 676 “Particles, Strings, and the Early Universe” at the University of Hamburg. JC is Royal Academy of Science Fellow financed by a grant of the Knut and Alice Wallenberg foundation.

A Error on the Poisson anisotropy

The error on the *fluctuation* angular power spectrum is given by

$$\delta C_\ell \equiv \sigma_\ell = (C_\ell + C_N w_\ell^2) \sqrt{\frac{2}{f_{\text{sky}}(2\ell + 1)}}, \quad (\text{A.1})$$

where $C_N = \Omega_{\text{fov}}(1/N_\gamma + N_b/N_\gamma^2)$ is the (Poissonian) noise, N_γ the number of gamma-ray events, N_b the number of background events, and Ω_{fov} the total fov in steradians [8]; $w_\ell = \exp(\sigma_{\text{psf}}^2 \ell(\ell + 1)/2)$ describes the correction for a Gaussian PSF of width σ_{psf} (in radians). In the following derivation of the sensitivity, we assume a Poisson-like power spectrum, i.e. $C_\ell = C_P$. In practice, C_P is estimated by calculating the weighted average of the measured angular power spectrum, so that $C_P = \sum_\ell p_\ell C_\ell$, where $p_\ell = (1/\sigma_\ell^2)/(\sum_\ell 1/\sigma_\ell^2)$ (the weight of higher multipoles is larger, owing to smaller errors until the PSF error starts to dominate). The corresponding error on C_P is the given by $(\delta C_P)^2 = \sum_\ell p_\ell^2 (\delta C_\ell)^2 = 1/(\sum_\ell 1/\sigma_\ell^2)$.

A.1 Simple calculation

In the following, we consider both a sufficiently narrow PSF, resulting in a sufficiently small PSF correction for the multipole range of interest, and the high statistics limit, so that C_N is negligible with respect to C_P . In this limit, we have (implicitly, $\ell \gg 1$ is assumed)

$$\sigma_\ell = C_\ell \sqrt{\frac{1}{f_{\text{sky}} \ell}}. \quad (\text{A.2})$$

Evaluating the sum in $(\delta C_P)^2 = 1/(\sum_\ell 1/\sigma_\ell^2)$ (this can be done analytically or approximating the sum as an integral) yields

$$\delta C_P \approx C_P \sqrt{\frac{2}{f_{\text{sky}}(\ell_{\text{max}}^2 - \ell_{\text{min}}^2)}} \approx \frac{C_P}{\ell_{\text{max}}} \sqrt{\frac{2}{f_{\text{sky}}}}. \quad (\text{A.3})$$

A.2 More accurate calculation

Assuming $\ell \gg 1$,

$$\sigma_\ell = (C_\ell + C_N w_\ell^2) \sqrt{\frac{1}{f_{\text{sky}} \ell}}. \quad (\text{A.4})$$

Evaluating the sum $(\delta C_P)^2 = 1/(\sum_\ell 1/\sigma_\ell^2)$ by approximating it as an integral we find

$$\delta C_P \approx \sqrt{\frac{1}{f_{\text{sky}}}} \left(-\frac{\ell_{\text{min}}^2}{C_P^2} - \frac{\ln(C_P/C_N + w_{\ell_{\text{min}}}^2)}{C_P^2 \sigma_{\text{psf}}^2} - \frac{1}{2 C_P \sigma_{\text{psf}}^2 (C_P + C_N w_{\ell_{\text{min}}}^2)} \right)^{-\frac{1}{2}}. \quad (\text{A.5})$$

With $\ell_{\text{min}} \approx 100$, $\sigma_{\text{psf}} = 0.05^\circ \ll 1/\ell_{\text{min}} \approx 0.6^\circ$, and in the limit of high statistics ($C_P \gg C_N$), the expression can be simplified as

$$\delta C_P \approx C_P \sigma_{\text{psf}} \sqrt{\frac{2}{f_{\text{sky}} \ln\left(\frac{C_P}{e C_N}\right)}} \equiv \frac{C_P}{\ell_{\text{max}}} \sqrt{\frac{2}{f_{\text{sky}}}}, \quad (\text{A.6})$$

which is equivalent to the previous simplified calculation with the definition $\ell_{\text{max}} = \sigma_{\text{psf}}^{-1} \sqrt{\ln\left(\frac{C_P}{e C_N}\right)}$. Note that the quantity $\ln\left(\frac{C_P}{e C_N}\right)$ is of order ~ 1 in the high statistics limit. In the case discussed in the paper, $\sigma_{\text{psf}} = 0.05^\circ$ is assumed, so that the first condition is satisfied. Further, a fov of 5° corresponds to $\Omega_{\text{fov}} \approx 10^{-2}$ sr and $f_{\text{sky}} \approx 10^{-3}$. Given a 1000 h observation and a background rate of 10 Hz above 100 GeV, $C_N \approx 3 \times 10^{-5}$, referring to the number of events in table 2, while the case for 1 Hz above 300 GeV corresponds to $C_N \approx 8 \times 10^{-6}$, both to be compared with $C_P = 10^{-5}$. Therefore, we face the condition $C_P \sim C_N$ even for the most optimistic cases. Nonetheless, for illustration purposes, the following derivation focusses on the regime $C_P \gg C_N$, estimating the sensitivity achievable under optimal conditions.

B Sensitivity using the intensity APS

More convenient calculations can be carried out in terms of the intensity APS, since power spectra are linearly additive in case of uncorrelated summands. This is indeed the case for Poisson-like anisotropies.

The intensity APS is simply related to the fluctuation APS as

$$C_P^I = I^2 C_P, \quad (\text{B.1})$$

where I is the intensity of the considered component. We consider the same scenario as above, i.e. an astrophysical component with Poissonian anisotropy C_A and intensity I_A , and a DM component with anisotropy C_{DM} and intensity I_{DM} . The corresponding intensity anisotropies are given by $C_A^I = I_A^2 C_A$ and $C_{DM}^I = I_{DM}^2 C_{DM}$. Assuming that the intensity anisotropy $C_P^{I,\text{data}} \pm \delta C_P^{I,\text{data}}$ has been measured in a given energy band, we can set a conservative upper limit on the DM contribution as

$$C_{DM}^I \lesssim C_P^{I,\text{data}}, \quad (\text{B.2})$$

which implies

$$\frac{I_{DM}}{I} \lesssim \sqrt{\frac{C_P^{\text{data}}}{C_{DM}}}. \quad (\text{B.3})$$

If the DM component is subdominant, we have $C_P^{\text{data}} \sim C_A$ and $I_{DM}/I \lesssim \sqrt{C_A/C_{DM}}$. For the benchmark case with $C_A = 10^{-5}$ and $C_{DM} = 10^{-3}$, this yields a maximum sensitivity of $I_{DM}/I \lesssim 10\%$.

A case more accurately approximating the case discussed with the previous simulations is given when the quantity $C_P^{I,\text{data}} = C_A^I$ is known within a certain error in advance, either because we have measured this quantity in a different energy band, or because it matches our theoretical expectations. In this case, a more interesting upper limit can be derived from

$$C_{DM}^I \lesssim \delta C_P^{I,\text{data}}, \quad (\text{B.4})$$

which implies

$$\frac{I_{DM}}{I} \lesssim \sqrt{\frac{C_P^{\text{data}}}{C_{DM}}} \times \sqrt[4]{\frac{2}{f_{\text{sky}} \ell_{\text{max}}^2}}. \quad (\text{B.5})$$

Again, with $C_P^{\text{data}} = C_A$ and for our benchmark case $C_A = 10^{-5}$, $C_{DM} = 10^{-3}$, $\ell_{\text{max}} \approx 1000$, and $f_{\text{sky}} \approx 10^{-3}$, we have a maximum sensitivity of $I_{DM}/I \lesssim 2\%$. Note that the sensitivity improves with a larger fov, although only with the fourth root. However, the sensitivity improves faster with the angular resolution (ℓ_{max}).

We emphasize that the above results are clearly back-of-the-envelope calculations, with the purpose of estimating the sensitivity and its dependence on the relevant quantities. Dealing with real data, more appropriate derivations can be conducted, for example, with a likelihood analysis.

C Sensitivity using the fluctuation APS

In the paper, fluctuation anisotropies are used to calculate the sensitivities. In this case, the relation effectively imposed to derive the sensitivity is

$$C_P^{\text{data}} - \delta C_P^{\text{data}} \lesssim C_{\text{tot}} \lesssim C_P^{\text{data}} + \delta C_P^{\text{data}}, \quad (\text{C.1})$$

where

$$C_{\text{tot}} = \frac{C_{DM} I_{DM}^2 + C_A I_A^2}{(I_{DM} + I_A)^2}. \quad (\text{C.2})$$

Rewriting $C_P^{\text{data}} \pm \delta C_P^{\text{data}}$ as $C_P^{\text{data}} (1 \pm \Delta)$, where $\Delta \equiv \sqrt{2/(f_{\text{sky}} \ell_{\text{max}}^2)}$, we find that the sensitivity is given by a second order equation, solved by

$$\frac{I_{DM}}{I_A} = \frac{C_P^{\text{data}} (1 \pm \Delta) \pm \sqrt{C_P^{\text{data}} (1 \pm \Delta) (C_A + C_{DM}) - C_A C_{DM}}}{C_P^{\text{data}} (1 \pm \Delta) - C_{DM}}. \quad (\text{C.3})$$

The equation can be simplified in a few relevant cases. For example, if $C_{DM} \gg C_A$ (as in the benchmark case), and again assuming $C_P^{\text{data}} \approx C_A$, the positive (physical) solution is

$$\frac{I_{DM}}{I} \lesssim \frac{C_P^{\text{data}}}{C_{DM}} + \sqrt{\frac{C_P^{\text{data}}}{C_{DM}}} \sqrt[4]{\frac{2}{f_{\text{sky}} \ell_{\text{max}}^2}}. \quad (\text{C.4})$$

For the benchmark numbers, we get a sensitivity of $I_{DM}/I \lesssim 3\%$, only slightly worse than in the intensity case. Therefore, the actual value of 10% for the sensitivity quoted in the paper for the most favorable scenario is not very far from the analytical estimate.

For $C_A = 10^{-4}$ and $C_{DM} = 10^{-3}$ the above sensitivity degrades quite rapidly, worsening by a factor of 10, in agreement with the simulations performed. In the intensity case, instead, the dependence only goes with the square root, and the sensitivity should worsen by a factor of ~ 3 only.

Finally, unlike in the intensity case, we get an upper limit on I_{DM} , even in the case $C_{DM} \ll C_A$. This scenario is quite unphysical, although it can be practically taken as case study for a further (non-DM) component with negligible anisotropy. This is expected, for example, from normal galaxies or truly diffuse processes like photons from UHECRs cascades on the CMB. In this case, after a few simplifications we get

$$\frac{I_{DM}}{I} \lesssim \sqrt{\frac{2}{f_{\text{sky}} \ell_{\text{max}}^2}}, \quad (\text{C.5})$$

which is independent of C_A . The benchmark numbers for f_{sky} and ℓ_{max} yield a limit of $I_{DM}/I \lesssim 5\%$.

The case $C_A \sim C_{DM}$ seems to give the worst limit. For this regime, a simple formula cannot be derived and the full expression Eq. C.3 needs to be used.

References

- [1] M. Ackermann *et al.* [Fermi LAT Collaboration], Phys. Rev. D **85** (2012) 083007 [arXiv:1202.2856 [astro-ph.HE]].
- [2] A. Cuoco, E. Komatsu and J. M. Siegal-Gaskins, Phys. Rev. D **86** (2012) 063004 [arXiv:1202.5309 [astro-ph.CO]].
- [3] A. A. Abdo et al. [Fermi LAT Collaboration], Phys. Rev. Lett. **104** (2010) 101101.
- [4] C. D. Dermer, AIP Conf. Proc. **921** (2007) 122-126 [arXiv:0704.2888 [astro-ph]].
- [5] C. -A. Faucher-Giguere and A. Loeb, JCAP **1001** (2010) 005 [arXiv:0904.3102 [astro-ph.HE]].
- [6] D. Malyshev and D. W. Hogg, Astrophys. J. **738** (2011) 181 [arXiv:1104.0010 [astro-ph.CO]].
- [7] J. -Q. Xia, A. Cuoco, E. Branchini, M. Fornasa and M. Viel, Mon. Not. Roy. Astron. Soc. **416** (2011) 2247 [arXiv:1103.4861 [astro-ph.CO]].
- [8] S. Ando and E. Komatsu, Phys. Rev. D **73** (2006) 023521;
- [9] S. Ando, E. Komatsu, T. Narumoto and T. Totani, Phys. Rev. D **75** (2007) 063519;
- [10] A. Cuoco, S. Hannestad, T. Haugbolle, G. Miele, P. D. Serpico and H. Tu, JCAP **0704** (2007) 013 [astro-ph/0612559].
- [11] A. Cuoco, J. Brandbyge, S. Hannestad, T. Haugboelle and G. Miele, Phys. Rev. D **77** (2008) 123518;
- [12] J. M. Siegal-Gaskins, JCAP **0810** (2008) 040;
- [13] M. Fornasa, L. Pieri, G. Bertone, E. Branchini, Phys. Rev. **D80** (2009) 023518;
- [14] J. M. Siegal-Gaskins, V. Pavlidou, Phys. Rev. Lett. **102** (2009) 241301;
- [15] S. 'i. Ando, Phys. Rev. D **80** (2009) 023520 [arXiv:0903.4685 [astro-ph.CO]].
- [16] J. Zavala, V. Springel, M. Boylan-Kolchin, Mon. Not. Roy. Astron. Soc. **405** (2010) 593;
- [17] B. S. Hensley, J. M. Siegal-Gaskins, V. Pavlidou, Astrophys. J. **723** (2010) 277;
- [18] A. Cuoco, A. Sellaerholm, J. Conrad and S. Hannestad, Mon. Not. Roy. Astron. Soc. **414** (2011) 2040;
- [19] M. Fornasa, J. Zavala, M. A. Sanchez-Conde, J. M. Siegal-Gaskins, T. Delahaye, F. Prada, M. Vogelsberger and F. Zandanel *et al.*, MNRAS, 429, **1529** (2013) [arXiv:1207.0502 [astro-ph.HE]].
- [20] S. Ando, E. Komatsu, T. Narumoto and T. Totani, Mon. Not. Roy. Astron. Soc. **376** (2007) 1635; F. Miniati, S. M. Koushiappas and T. Di Matteo, Astrophys. J. **667** (2007) L1
- [21] J. M. Siegal-Gaskins, R. Reesman, V. Pavlidou, S. Profumo, T. P. Walker, Mon. Not. Roy. Astron. Soc. **415** (2011) 1074S.
- [22] S. Ando and V. Pavlidou, Mon. Not. Roy. Astron. Soc. **400** (2009) 2122
- [23] W. B. Atwood *et al.* [LAT Collaboration], Astrophys. J. **697**, 1071 (2009)

- [24] F. Aharonian *et al.* [H.E.S.S. Collaboration], *Astron. Astrophys.* **457** (2006) 899 [astro-ph/0607333].
- [25] J. Albert *et al.* [MAGIC Collaboration], *Astrophys. J.* **674** (2008) 1037 [arXiv:0705.3244 [astro-ph]].
- [26] E. Aliu *et al.* [VERITAS Collaboration], *Science* **334** (2011) 69 [arXiv:1108.3797 [astro-ph.HE]].
- [27] The CTA Consortium, arXiv:1008.3703 (2010).
- [28] M. Doro *et al.* [CTA Collaboration], *Astropart. Phys.* **43**, 189 (2013) [arXiv:1208.5356 [astro-ph.IM]].
- [29] F. A. Aharonian, A. K. Konopelko, H. J. Volk and H. Quintana, *Astropart. Phys.* **15** (2001) 335 [astro-ph/0006163].
- [30] A. A. Abdo *et al.* [Fermi LAT Collaboration], *Phys. Rev. Lett.* **102** (2009) 181101 [arXiv:0905.0025 [astro-ph.HE]].
- [31] M. Ackermann *et al.* [Fermi LAT Collaboration], *Phys. Rev. D* **82** (2010) 092004 [arXiv:1008.3999 [astro-ph.HE]].
- [32] F. Aharonian *et al.* [H.E.S.S. Collaboration], *Phys. Rev. Lett.* **101** (2008) 261104 [arXiv:0811.3894 [astro-ph]].
- [33] F. Aharonian *et al.* [H.E.S.S. Collaboration], *Astron. Astrophys.* **508** (2009) 561 [arXiv:0905.0105 [astro-ph.HE]].
- [34] G. P. Rowell, *Astron. Astrophys.* **410** (2003) 389 [astro-ph/0310025].
- [35] K. M. Gorski, E. Hivon, A. J. Banday, B. D. Wandelt, F. K. Hansen, M. Reinecke and M. Bartelman, *Astrophys. J.* **622** (2005) 759 [arXiv:astro-ph/0409513].
- [36] M. Ackermann *et al.* [Fermi-LAT Collaboration], *Phys. Rev. D* **82** (2010) 092003 [arXiv:1008.5119 [astro-ph.HE]].
- [37] M. Aguilar *et al.* [AMS Collaboration], *Phys. Rev. Lett.* **110**, no. 14, 141102 (2013).
- [38] R. Abbasi *et al.* [IceCube Collaboration], *Astrophys. J.* **740** (2011) 16 [arXiv:1105.2326 [astro-ph.HE]].
- [39] R. Abbasi *et al.* [IceCube Collaboration], *Astrophys. J.* **746** (2012) 33 [arXiv:1109.1017 [hep-ex]].
- [40] A. A. Abdo, B. Allen, T. Aune, D. Berley, E. Blaufuss, S. Casanova, C. Chen and B. L. Dingus *et al.*, *Phys. Rev. Lett.* **101** (2008) 221101 [arXiv:0801.3827 [astro-ph]].
- [41] A. A. Abdo, B. T. Allen, T. Aune, D. Berley, S. Casanova, C. Chen, B. L. Dingus and R. W. Ellsworth *et al.*, *Astrophys. J.* **698** (2009) 2121 [arXiv:0806.2293 [astro-ph]].
- [42] S. Vernetto *et al.* [ARGO-YBJ Collaboration], *Proceedings of the 31 ICRC Conference, Lodz, Poland 2009*, [arXiv:0907.4615 [astro-ph.HE]].
- [43] J. Masbou, G. Lamanna and S. Rosier-Lees for the H.E.S.S. Collaboration, *Proceedings of the 31 ICRC Conference, Lodz, Poland 2009*, <http://icrc2009.uni.lodz.pl/proc/pdf/icrc1059.pdf>
- [44] K. Bernlohr, A. Barnacka, Y. Becherini, O. B. Bigas, E. Carmona, P. Colin, G. Decerprit and F. Di Pierro *et al.*, *Astropart. Phys.* **43**, 171 (2013) [arXiv:1210.3503 [astro-ph.IM]].

- [45] M. Martinez *et al.* [CTA Consortium Collaboration], [arXiv:1111.2183 [astro-ph.IM]].
- [46] A. Dominguez, J. R. Primack, D. J. Rosario, F. Prada, R. C. Gilmore, S. M. Faber, D. C. Koo and R. S. Somerville *et al.*, MNRAS, 410, **2556** (2011) [arXiv:1007.1459 [astro-ph.CO]].
- [47] J. D. Finke, S. Razzaque and C. D. Dermer, Astrophys. J. **712** (2010) 238 [arXiv:0905.1115 [astro-ph.HE]].
- [48] A. Franceschini, G. Rodighiero and M. Vaccari, Astron. Astrophys. **487** (2008) 837 [arXiv:0805.1841 [astro-ph]].
- [49] R. C. Gilmore, R. S. Somerville, J. R. Primack and A. Dominguez, MNRAS, 422, **3189** (2012) [arXiv:1104.0671 [astro-ph.CO]].
- [50] T. M. Kneiske and H. Dole, Astron. Astrophys. **515** (2010) A19 [arXiv:1001.2132 [astro-ph.CO]].
- [51] F. W. Stecker, M. A. Malkan and S. T. Scully, Astrophys. J. **761**, 128 (2012) [arXiv:1205.5168 [astro-ph.HE]].
- [52] M. Meyer, M. Raue, D. Mazin and D. Horns, Astron. Astrophys. **542** (2012) A59 [arXiv:1202.2867 [astro-ph.CO]].
- [53] A. A. Abdo *et al.* [Fermi-LAT Collaboration], Astrophys. J. **720** (2010) 435 [arXiv:1003.0895 [astro-ph.CO]].
- [54] P. Ullio, L. Bergstrom, J. Edsjo and C. G. Lacey, Phys. Rev. D **66**, 123502 (2002) [arXiv:astro-ph/0207125].
- [55] H.-S. Zechlin, M. V. Fernandes, D. Elsaesser and D. Horns, Astron. Astrophys. **538** (2012) A93 [arXiv:1111.3514 [astro-ph.HE]].
- [56] H.-S. Zechlin and D. Horns, JCAP **1211** (2012) 050 [arXiv:1210.3852 [astro-ph.HE]].
- [57] A. A. Abdo *et al.* [Fermi-LAT Collaboration], arXiv:1002.4415 (2010a).